# Influence of laser processing parameters on microstructure and defect formation in PBF-LB printed Al-Si-Mg alloys

*Lerato* Semetse[1*], *Yanelisa Nelly* Godlo[1], *Olayinka* Olaogun[1,2], and *Peter Apata* Olubambi[1]

[1]Centre for Nano-engineering and Advanced Materials, School of Mining, Metallurgy and Chemical Engineering, University of Johannesburg, South Africa
[2]University West, Department of Mechanical Engineering Science, Division of Welding Technology (KAMPT), Sweden

**Abstract.** The performance and reliability of additively manufactured Al-Si-Mg parts are strongly influenced by processing parameters, which affects microstructure and defect formation. This study examines five scanning speeds using powder bed fusion – laser beam (PBF-LB) and analyses porosity, grain morphology, and crystallographic texture via SEM and X-ray diffraction. Higher scanning speeds led to increased porosity and incomplete fusion, while lower scanning speeds produced refined columnar grains and continuous eutectic silicon networks due to prolonged thermal exposure. Phase analysis confirmed α-Al as the dominant matrix phase, with presence of intermetallics and oxides reflecting thermal history and potential contamination. Crystallographic texture analysis showed that reduced scanning speeds enhanced grain orientation and residual stress. Intermediate scanning conditions minimized defects while preserving desirable microstructural characteristics. This study gives insights into process-structure relationships, supporting parameter optimization for high performance application of Al-Si-Mg alloys in aerospace and automotive sectors.

## 1 Introduction

Additive manufacturing (AM), especially metal-based techniques, have transformed the production of complex and high-performance components across multiple industries such as aerospace and automotive industry. Among these techniques, Powder Bed Fusion- Laser Beam (PBF-LB), as defined by the ISO/ASTM 52900 standard [1], has drawn significant attention due to its precision, efficiency, and ability to fabricate intricate geometries. In PBF-LB, a high-powered laser selectively melts layers of metal powder based on a digital model, enabling the layer-by-layer manufacture of intricate components. This process is especially suited for lightweight structural applications in aerospace, automotive, and biomedical sectors due to its capability to produce parts with high dimensional accuracy [2].

Al-Si-Mg alloy, a casting alloy belonging to the Al-Si (4xxx) series, is among the most widely utilized alloys in PBF-LB process due to its favourable solidification behaviour and mechanical properties [3]. These alloys are recognized for their high strength to weight ratio,

excellent thermal conductivity, and corrosion resistance. The adoption of Al-Si-Mg in AM processes as stated by [4] is driven by its ability to combine structural performance with low density. In addition, the characteristic microstructure of the cellular α-Al grains enveloped by eutectic silicon networks enhances mechanical strength and wear resistance in as-built components.

Despite these advantages, the PBF-LB processing of Al-Si-Mg alloys remains challenged by process induced defects and microstructural inhomogeneity, similar to those observed in other additively manufactured metals. Achieving optimal performance requires precise control of process parameters such as laser power, scanning speed, hatch spacing, and layer thickness. Variations in these parameters significantly influence thermal gradients, melt pool stability, solidification rates, and resulting phase formation and crystallographic texture [5]. According to Pan et al. [6], scanning speed is pivotal, as it directly governs the energy input per unit length, thereby influencing melt pool geometry and cooling rate. The combined effect of laser power, scanning speed, hatch spacing, and layer thickness is often represented by the volumetric energy density [7]. High scanning speeds often result in insufficient melting and poor fusion between adjacent layers, leading to increased porosity and surface roughness [7]. In contrast, excessively low scanning speeds may cause excessive heat buildup, inducing keyhole defects, residual stress accumulation, and grain coarsening [2]. The grain structure of PBF-LB printed Al-Si-Mg alloys is majorly influenced by directional solidification, where the grains tend to grow along the build direction due to vertical heat flow. Depending on the thermal gradient and cooling rate, this can result in either columnar or equiaxed grain structures [8]. As reported by Hadadzadeh et al. [9], the formation of columnar grains aligned with the thermal gradient fosters a highly textured microstructure, contributing to anisotropic mechanical behaviour. Moreover, the repeated melting and re-solidification cycles inherent to layer-by-layer fabrication can modulate eutectic silicon morphology and redistribute particles along melt pool boundaries [10].

Crystallographic texture is crucial in determining the directional dependence of mechanical and physical properties in additively manufactured alloys. In PBF-LB processes, the thermal history during processing influences not only the grain morphology but also the crystallographic orientation of the α-Al matrix. Preferred orientations can develop due to epitaxial growth, with dominant texture components often observed along the (100) and (110) planes, depending on the energy density and solidification dynamics. Energy density, commonly expressed as volumetric energy density, is defined as the ration of laser power to the product of scanning speed, hatch spacing and layer thickness [11]. These textures can impact anisotropic yield behaviour, fatigue resistance, and corrosion performance especially in critical applications. This occurs because preferred crystallographic orientations determine the directionality of slip systems and dislocation motion in the α-Al matrix [12]. Similarly, directional alignment of grains and eutectic networks contributes to localized cyclic strain accumulation during service, thereby influencing fatigue crack initiation and propagation pathways [13]. In terms of corrosion behaviour, the orientation dependent distribution of intermetallic phases and residual stress fields can promote galvanic cells and accelerate localized attack, particularly at grain boundaries exposed to aggressive environments [14].
While existing literature provides a foundation for understanding the mechanical and thermal behaviour of Al-Si-Mg in additive manufacturing, a detailed correlation between scanning speed and resultant microstructural evolution and phase transformation remains underexplored. Furthermore, few studies isolate scanning speed as the sole variable, with other parameters held constant.

Therefore, this study presents investigation of the microstructure, phase formation, and crystallographic texture of Al-Si-Mg specimens printed via PBF-LB under five distinct scanning speeds ranging from 1815 mm/s to 1485 mm/s. The aim is to elucidate the influence

of scanning speed on solidification behaviour, porosity characteristics, grain refinement, secondary phase formation, and texture evolution.

## 2 Materials and methods

### 2.1 Materials and PBF-LB processing

In this study, SLM®280 PBF-LB system (SLM Solutions, Lubeck, Germany) was utilized, depicted in Fig. 1, at METALHEART additive manufacturing services, South Africa.


**Fig.1.** SLM®280 LPBF system and cross-sectioned as-built Al-Si-Mg cylindrical specimen.

The Laser Beam Powder Bed Fusion (PBF-LB) process was employed to fabricate Al-Si-Mg cylindrical samples, with Autodesk Fusion used to generate the desired geometry. Virgin Al-Si-Mg powder, supplied by METAL 3DP, consisted of spherical, highly flowable particles with a size range of 20 to 63 µm, shown in Fig.2. Table 1 shows the chemical composition of the Al-Si-Mg alloy powder. The alloy is aluminium-based, with silicon as the main addition (9.7 wt.%), magnesium (0.43 wt.%), and minor elements such as Mn (0.45 wt.%) and Fe (0.55 wt.%). Trace levels of Cu, Ni, Zn, and Ti are also present, consistent with standard Al-Si-Mg alloys used in PBF-LB.

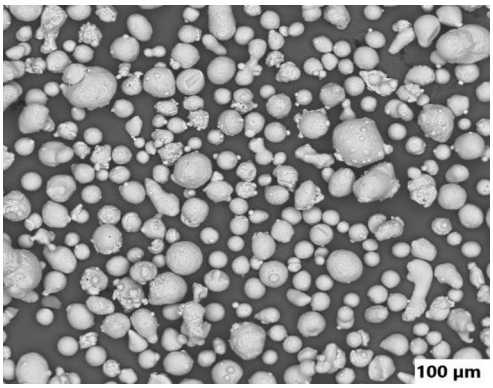


**Fig.2.** SEM micrograph of supplied Al-Si-Mg powder showing predominant spherical particles.

**Table 1.** Elemental composition of Al-Si-Mg (weight %).

| Element | Si | Mg | Cu | Mn | Ni | Fe | Zn | Ti | Al |
|---|---|---|---|---|---|---|---|---|---|
| Weight % | **9.700** | **0.430** | **0. 050** | **0.450** | **0.035** | **0.550** | **0.100** | **0.150** | **Balance** |

The layer deposition employed a 15º rotational scanning strategy between successive layers, with a hatch distance of 0.1 mm corresponding to a 40% overlap between adjacent scan tracks. To prevent oxidation during the rapid heating and cooling cycles, argon gas was used for shielding at a flow rate of 8 L/min. The as-built 3D solid cylindrical-shaped Al-Si-Mg specimens, each with a diameter of 9.8 mm and height of 30 mm, were fabricated using the processing parameters outlined in Table 2. To investigate the influence of the volumetric energy density on part quality and microstructural evolution, the scanning speed was systematically varied by ±5% and ±10% relative to the manufacturer recommended baseline of 1650 mm/s. This variation enabled exploration of energy densities within the typical optimal range of 30-60 J/mm$^3$ for Al-Si-Mg alloys. The samples were wire cut longitudinally and hot mounted for further characterization.

**Table 2.** PBF-LB processing parameters.

| Parameter | Value |
|---|---|
| Laser Power (W) | 370 |
| Layer thickness (µm) | 60 |
| Hatch distance (µm) | 100 |
| Scan speed (mm/s) | 1485, 1567, 1650, 1732, 1815 |

## 2.2 Morphological characterization

The 3D-printed cylindrical-shaped Al-Si-Mg samples underwent metallographic preparation prior to Scanning Electron Microscopy (SEM) and XRD analysis. After fabrication via PBF-LB, the specimens were ultrasonically cleaned in ethanol to eliminate residual powder particles and surface contaminants. The transverse wire cut specimens were hot mounted, grinded, and polished to achieve a mirror-like surface, following Struers application procedures for aluminium alloys [15]. The specimens underwent mechanical polishing using silicon carbide abrasive sheets progressing from 600 to 4000 grit, ensuring a smooth and reflective surface appropriate for diffraction measurements. The cross-sectional microscopy analysis was performed before and after etching with Keller's reagent using a field-emission scanning electron microscope (FESEM) JEOL JSM 7900F, equipped with Oxford Instrument EDS hardware and featuring a secondary electron imaging (SEI) resolution of 30 kV. The phase composition and crystallographic characteristics of the 3D printed Al-Si-Mg alloy specimens were examined using X-ray diffraction (XRD). A PANalytical X'Pert PRO diffractometer with a Cu Kα radiation source (λ = 1.5406 Å) and an accelerating voltage of 40 kV and a current of 40 mA was used to perform XRD measurements. Step size was 0.02°, dwell time was 1 s per step, and the diffraction data were obtained in the θ–2θ configuration throughout a scan range of 5°–90° (2θ). To improve peak resolution, minimize background noise, and improve diffraction clarity, a graphite monochromator and a fixed divergence slit were utilized. The phase composition and crystallographic characteristics of the 3D printed Al-Si-Mg alloy specimens were identified using the diffraction pattern analysis.

# 3 Results and discussion

## 3.1 Microstructure and defects detection

Figure 3 illustrates the metallurgical morphology and defects dispersion of PBF-LB printed Al-Si-Mg samples produced at different scanning speeds in magnification of x500. The scanning speeds, designated as samples A, B, C, D, and E are 1815 mm/s, 1732 mm/s, 1650 mm/s, 1567 mm/s, and 1485 mm/s, respectively. Porosity in PBF-LB components arises from a range of process induced phenomena. While previous studies [16,17] have identified entrapped inert gases and lack of fusion between layers as common sources, recent literatures reveal a broader spectrum of pore formation mechanism. These include keyhole instability, powder morphology defects, balling effects, and solidification cracking, all contributing to void formation under varying process conditions [18-20]. Defects are classified as pores when they constitute enclosed voids within the solidified matrix formed during melting and solidification. Pores in PBF-LB components are classified as gas-induced, keyhole and lack of fusion pores based on their morphology, size and spatial distribution. Lack of fusion pores arises when insufficient energy input leads to incomplete melting and poor metallurgical bonding between layers [21]. ImageJ software was employed to analyse the porosity and the subsurface defects in the unetched SEM images of the samples, enabling precise quantification of porosities. The pore distribution across samples at varying scanning speeds reveals distinct differences. These porosity values represent the area fraction of pores relative to the total analysed area, thereby indicating the proportion of voids within a given space. Sample A exhibits the highest porosity (0.85%) with a mean pore size of 0.224 μm, which reflects a large number of relatively small pores formed due to insufficient melting at the highest scanning speed (1815 mm/s). Sample B presents the lowest porosity (0.27%) with the smallest mean pore size of 0.057 μm, suggesting improved fusion at intermediate energy input. In contrast, Sample C shows a porosity of 0.48% but the largest mean pore size of 1.326 μm, implying fewer but larger pores, likely associated with localized melt pool instabilities at 1650 mm/s. Samples D and E show intermediate porosities of 0.37% and 0.34% with mean pores sizes of 0.233 μm and 0.198 μm, respectively. Overall, these results indicate that scanning speed not only affects the size of individual pores but also influences the porosity percentage, as a function of the resulting volumetric energy density. This reflects the interplay between energy input, melt pool stability, and fusion behaviour during the PBF-LB process. The occurrence of bright, irregular structures observed across all micrograph samples indicates unmolten regions, which result from incomplete fusion. This defect arises when the laser energy input is insufficient to fully melt the powder, leading to weak metallurgical bonding between adjacent layers. While insufficient laser absorption is a primary cause, incomplete fusion is also affected by other process parameters such as hatch spacing, layer thickness, and laser spot size. These variables collectively determine the volumetric energy density. Therefore, achieving complete fusion requires balanced optimization of these parameters to ensure consistent energy delivery and stable melt pool dynamics throughout the build.

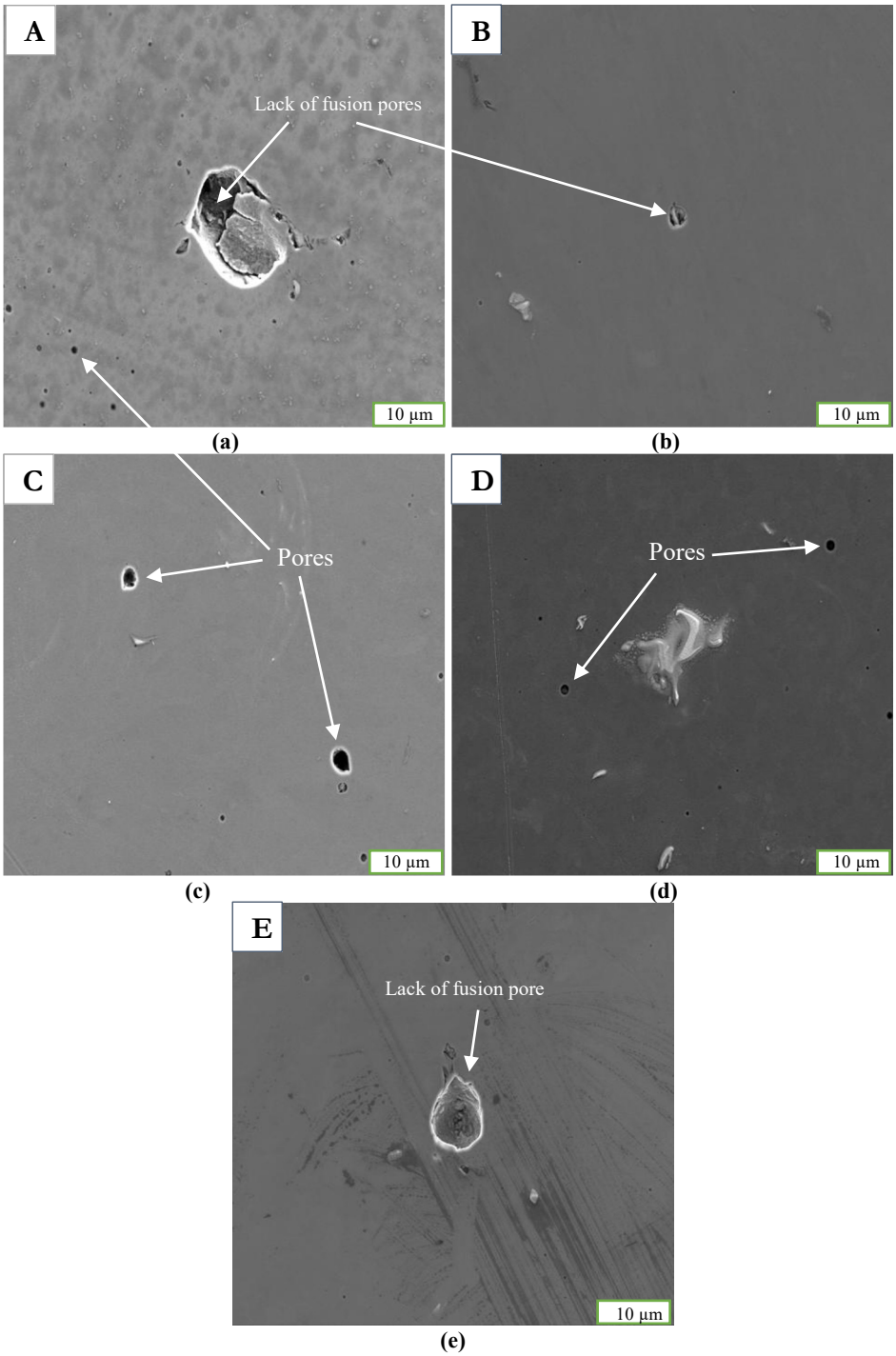


**Fig.3.** SEM micrographs showing metallurgical morphology and defects dispersion of PBF-LB printed Al-Si-Mg samples processed at different scanning speeds (a) 1815 mm/s, (b) 1732 mm/s, (c) 1650 mm/s, (d) 1567 mm/s, and (e) 1485 mm/s.

According to Maamoun et al. [22] and Prashanth et al. [23], the microstructure of as-built Al-Si-Mg is significantly influenced by the formation mechanism known as the particle-accumulated structure. This feature is characteristic of near eutectic aluminium alloys processed via PBF-LB, where rapid solidification promotes silicon segregation along cellular boundaries. While similar segregation phenomena may occur in other alloy systems, the particle-accumulated structure is most prominently associated with Al-Si-Mg compositions due to their unique eutectic solidification behaviour and high cooling rates. Under rapid cooling conditions inherent in laser powder bed fusion, this mechanism promotes the formation of a fibrous silicon network enveloping the aluminium matrix grain boundaries – a feature consistently observed across all scanning speeds, as shown in Figure 3. Notably, Sample A in Figure 4(a) reveals elongated grains, indicative of directional solidification governed by the prevailing thermal gradients and laser scan strategy. The observed transition from fine to coarser and irregular grain morphologies can be attributed to melt pool instability, and localized thermal cycling, both influenced by scanning speed. Lower speeds increase energy input and promote re-melting, leading to slower cooling and grain coarsening. In contrast, higher speeds reduce energy density, resulting in finer grains but a greater risk of incomplete fusion. Similarly, in Sample B - Figure 4(b), a predominant interconnected silicon-rich eutectic network and elongated grain structures are observed, confirming directional solidification aligned with the laser-induced thermal gradient. However, a distinct transition in melt pool morphology is evident, characterized by more columnar, aligned grain structures and a reduction in the branching of the eutectic network, indicating stronger directional solidification. Heat affected zones (HAZ), characterized by a discontinuous or fragmented Si network, can also be observed along the melt pool. HAZ form as a result high thermal cycles induced during successive melting of powder layers. Moreover, Sample C reveals a densely packed and interconnected eutectic silicon network, characteristic of rapid cooling and solidification. Compared to Samples A and B, Sample C displays a more refined columnar grain structure. This observation aligns with the findings of Maamoun et al. [22], who reported that reduced scan speeds in PBF-LB processing promote refined grains and interconnected eutectic silicon due to intensified thermal gradients and increased undercooling. In the lower region of Sample C, pronounced elongated grains aligned with the heat flow direction are evident, reflecting directional solidification along the build orientation. Additionally, distinct radial grain growth at the bottom center indicates a melt pool boundary. This feature aligns with the description by Liu et al. [24], who observed that melt pool boundaries are often associated with heterogeneous cellular-dendritic growth and complex eutectic patterns resulting from partial remelting and uneven heat distribution.

In Sample D - Figure 4(d), the microstructure continues the trend toward refinement as scanning speed decreases. A clearly defined and uniformly distributed eutectic silicon network is observed, with elongated cellular structures aligned predominantly in the build direction. These features indicate a more stable thermal gradient, and reduced scan-induced disturbances compared to the higher-speed Samples A and B. The longitudinal section reveals fewer disrupted regions and minimal evidence of remelting, suggesting optimized thermal conditions that promote directional solidification. This morphology aligns with the findings of Liu et al. [24], who highlighted that moderate scanning speeds stabilize melt pool dynamics and enhance columnar growth parallel to heat flux.

Sample E, shown in Figure 4(e), produced at the lowest scanning speed of 1485 mm/s, exhibits the most refined and continuous eutectic silicon network, characterized by a pronounced columnar grain orientation. The microstructure is densely packed, uniform, and displays reduced evidence of melt pool re-solidification. This refined grain morphology observed is attributed to prolonged laser-material interaction, which results in enhanced energy input and reduced cooling rates. This extended exposure can also intensify thermal

gradients and cyclic reheating, which are contributors to residual stress in PBF-LB builds [25]. Furthermore, literature also suggests that sustained directional solidification and the formation of uniform columnar grains may contribute to partial stress redistribution by stabilizing the microstructure [26]. Compared to Samples A-D, Sample E demonstrates the strongest expression of directional solidification along the build direction, exhibiting high degree of silicon network continuity. These findings indicate that the refined columnar morphology observed at lower scanning speeds reflects a balance between increased residual stress due to slower cooling and improved microstructural stability arising from enhanced grain continuity. Overall, the progression from Sample A to Sample E highlights the complex interplay between scan speed and microstructural evolution in PBF-LB processed Al-Si-Mg alloys. Higher scanning speeds (Samples A, B) yield finer cellular microstructures, with Sample B exhibiting the lowest porosity percentage suggesting a balance between energy input and defect restraint. However, these conditions may also introduce thermal instability and limit grain continuity. In contrast, lower scanning speeds (Samples D, E) offer microstructural uniformity and directional solidification, despite defects like lack of fusion due to excessive energy input and slower cooling. Sample C, at intermediate speed, reflects moderate refinement and aligned grain microstructure but may not outperform Sample B in terms of defect minimization. Importantly, the as-built microstructure across all samples remains amenable to post-processing for further refine grain morphology, redistribute silicon phases, and enhance mechanical properties by mitigating residual stress and improving ductility.

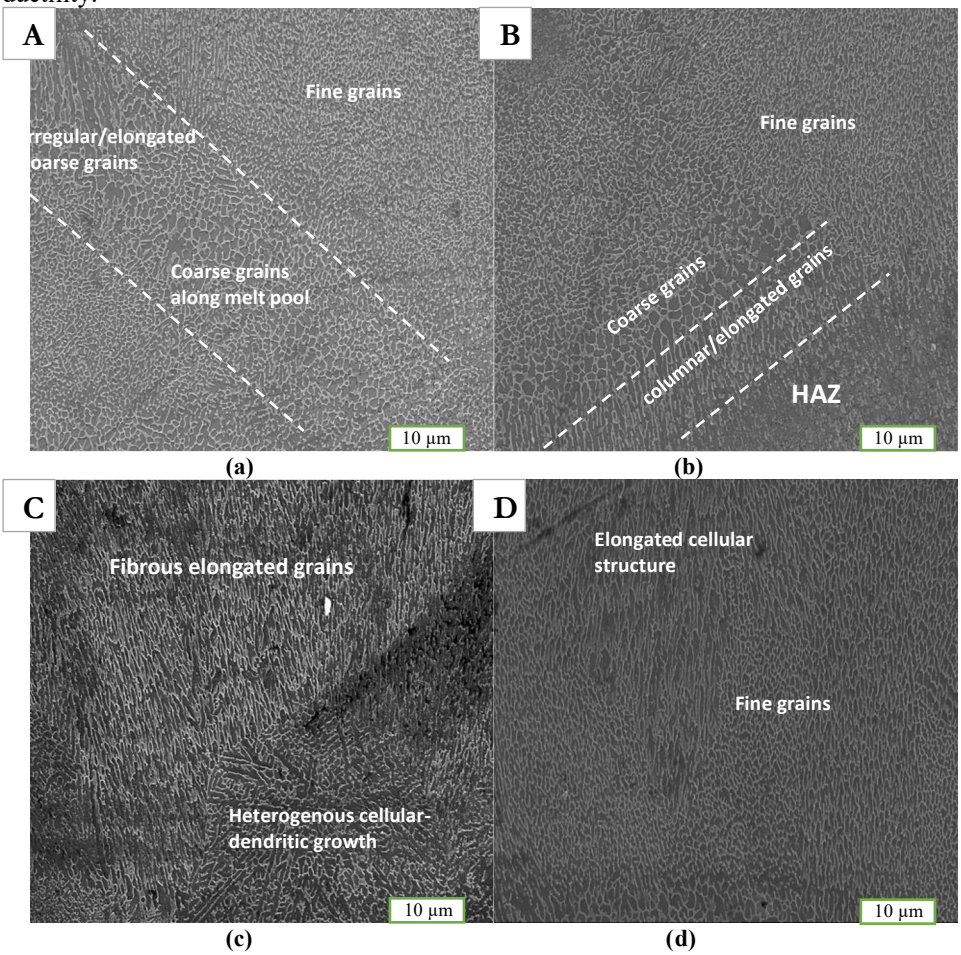

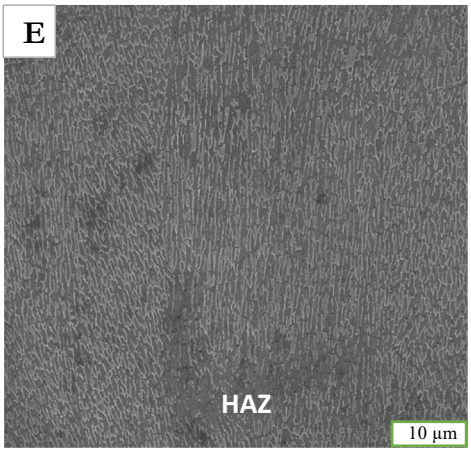


**(e)**

**Fig.4.** SEM micrographs showing grain morphology of PBF-LB printed Al-Si-Mg samples processed at different scanning speeds (a) 1815 mm/s, (b) 1732 mm/s, (c) 1650 mm/s, (d) 1567 mm/s, and (e) 1485 mm/s.

### 3.2 Phase identification

Figure 5 depicts the X-ray diffraction (XRD) patterns for PBF-LB printed Al-Si-Mg samples produced at varying scanning speeds. Across all scanning speeds, the dominant α-Al reflections were consistently observed at ~38.1° and 44.3° (2θ), corresponding to the (111) and (200) planes, confirming the persistence of the FCC aluminium matrix. Variations in peak intensity ratios between (111) and (200) indicate differences in preferred orientation, with stronger (111) planes emerging at lower scanning speeds. Peak broadening, reflected in higher FWHM values, was most pronounced at higher scanning speeds, especially in Sample A, suggesting finer crystallite domains and greater residual strain due to rapid solidification. Conversely, lower scanning speeds (Samples D and E) exhibited sharper and more intense peaks, consistent with coarser, columnar grains and stronger texture anisotropy. Intermediate scanning speed (Sample C) produced relatively balanced peak widths and intensities, indicative of refined yet well-aligned grain structures.

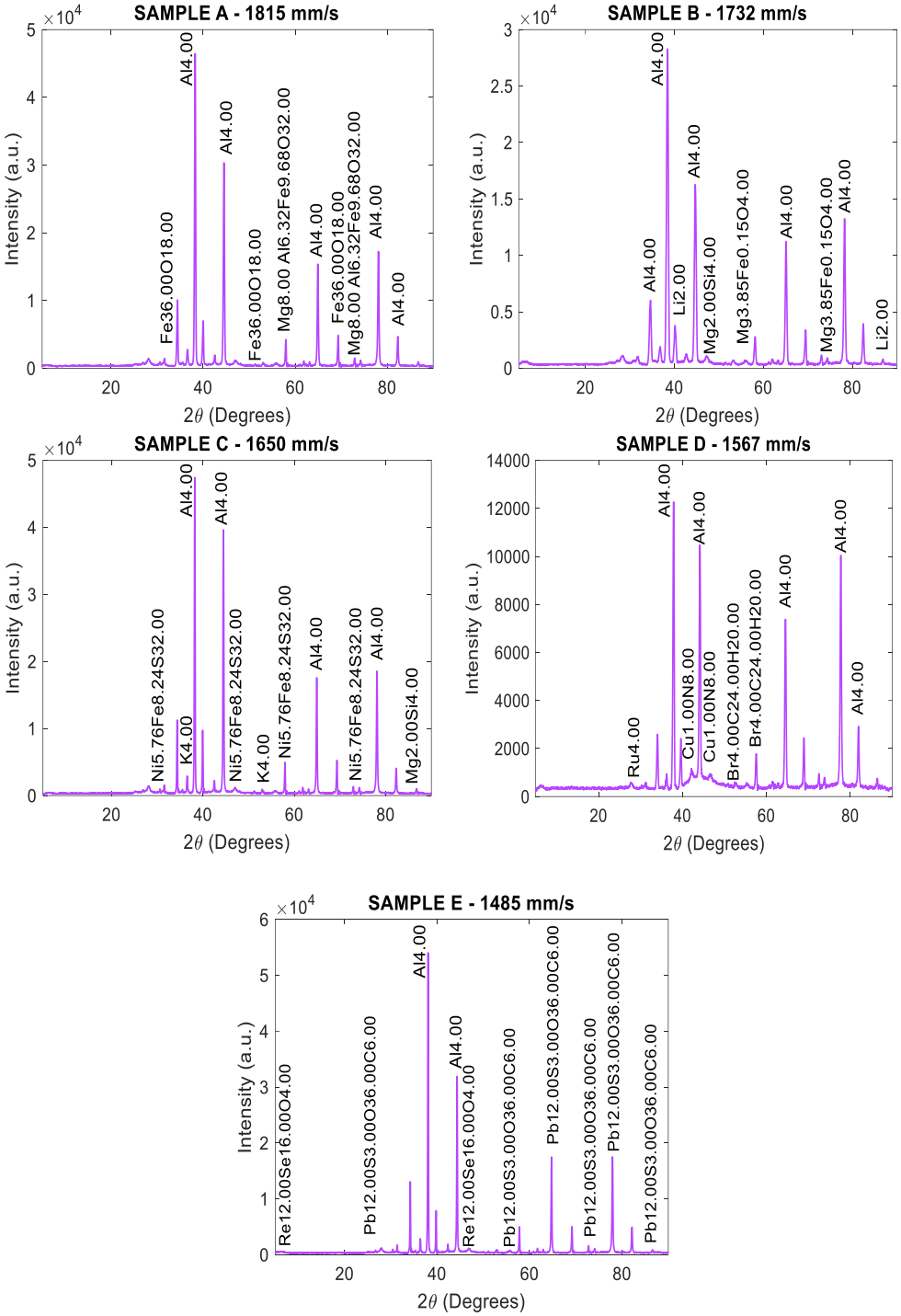


**Fig.5.** XRD patterns of PBF-LB printed Al-Si-Mg samples processed at different scanning speeds: A - 1815 mm/s, B - 1732 mm/s, C - 1650 mm/s, D - 1567 mm/s, and E - 1485 mm/s.

Across all samples, the dominant phase identified is the α-Al matrix, consistent with the face-centered cubic (FCC) structure. This is confirmed by the high intensity reflections at

approximately 2θ ~ 38.1º and 44.3º, corresponding to the (111) and (200) crystallographic planes respectively. The prevalence of α-Al across the samples aligns with the findings of Chowdhury et al [27], who also reported prominent aluminium matrix peaks at similar 2θ positions in PBF-LB printed Al-Si-Mg alloy. Although the build chamber was flooded with argon to minimize oxidation, the detection of magnesioferrite ($Mg_{8.00}$ $Al_{6.32}Fe_{9.68}O_{32.00}$), vermiculite ($Mg_{12}O_{48}Si_{16}$), and hematite ($Fe_{36}O_{18}$) phases in Samples A indicates that oxidation or impurity incorporation still occurred. This can be attributed to residual oxygen within the chamber atmosphere, improperly handled powders, and redeposition of spatter particles that readily oxidize during laser processing [28]. While standard powder handling procedures were reportedly followed at the METALHEART manufacturing site, these findings suggest that powder reuse and chamber trace oxygen levels may have contributed to the observed secondary phases formation. Sample B, similarly, shows α-Al as the primary phase, with (111) and (200) reflections at ~ 38.1º and 44.3º 2θ. The detection of magnesioferrite again points to oxidative effects during laser melting. Furthermore, the appearance of silicate-based compounds suggests solute segregation due to rapid solidification, a common occurrence in PBF-LB of aluminium alloys. In Sample C, α-Al matrix remains the dominant phase, as indicated by its strong characteristic peaks. The emergence of silicon-rich intermetallics in this sample likely results from solute redistribution during the melt pool's rapid solidification. Additionally, the presence of Fe-based oxides suggests localized oxidation, which also may stem from improper powder handling, spatter redeposition, or residual oxygen within the build chamber [28]. Sample D also exhibits dominant α-Al peaks at ~ 38.1º and 44.3º, reaffirming the FCC matrix structure. However, the detection of ruthenium ($Ru_4$) and Cu-N based compounds is unusual and may indicate trace contamination, interactions with environmental gases, or unintended elemental inclusion during the melting process. These secondary phase formations, coupled with shifts in diffraction intensity, suggest changes in crystallographic texture. This aligns with the SEM observations of directional solidification, particularly at reduced scanning speeds. In Sample E, the α-Al matrix persists, but with a noticeable increase in secondary phase formation. A prominent phase identified is $Pb_{12}S_3O_{36}$, a lead-based oxide, which may reflect environmental contamination or degradation of recycled powder. These findings support the SEM evidence of porosity and fusion related defects, indicating compromised structural integrity at this processing condition.

### 3.3 Crystallographic texture

As discussed in section 3.2, the diffraction peaks at ~38.1° and 44.3° (2θ), corresponding to the (111) and (200) planes of α-Al, were consistently observed across all scanning speeds. The crystallographic texture evolution across the PBL-LB Al-Si-Mg samples fabricated at varying scanning speeds is observed as well in Figure 5. In Sample A, the high intensity diffraction peaks at approximately 38º and 44º 2θ, corresponding to the (111) and (200) planes of the α-Al phase, indicating a distinct preferential crystallographic orientation. This refers to a non-random alignment of grains, where certain crystallographic planes, such as (111) and (200) are more frequently aligned parallel to the build direction, a phenomenon commonly known as crystallographic texture. The moderate peak broadening observed suggests the presence of microstructural strain or grain refinement, likely induced by rapid solidification. Additionally, low- angle peak broadening (below 20º) points to residual stresses and local microstructural inhomogeneity, possibly resulting from incomplete fusion during rapid layer deposition. In sample B, the α-Al phase remains dominant, as confirmed by the persistence of strong reflections at 38º and 44º 2θ. Compared to Sample A, increased peak broadening is observed, indicating a higher degree of microstructural refinement and residual stress accumulation, likely associated with the slightly reduced scanning speed. The

broader peaks and subtle intensity shifts suggest enhanced grain orientation variability and a growing influence of directional solidification on texture formation. As the scanning speed decreases further in Sample C, the XRD pattern reveals an evolving crystallographic texture characterized by sharpened and more aligned reflections, particularly within the aluminium matrix. The detection of silicon-rich intermetallic phases may contribute to local strain fields and promote anisotropic grain growth. These developments imply a transition toward more pronounced grain alignment observed in Figure 4(c). In Sample D, texture anisotropy becomes more pronounced, with the characteristic α-Al peaks displaying increased asymmetry and intensity modulation. This is indicative of a stronger crystallographic orientation bias, likely driven by enhanced columnar grain growth as seen in Figure 4(d), under lower scanning speed condition. The emergence of secondary phases such as ruthenium and copper-based compounds introduces localized distortions in the lattice, further complicating the crystallographic texture. These features align with SEM observations of elongated grains and directional solidification patterns. Finally, in Sample E, printed at the lowest scanning speed, the XRD pattern reveals the strongest expression of preferential orientation. This is evidenced by significant peak broadening and modulation, suggesting a high degree of residual stress and microstructural strain due to prolonged thermal exposure and slow heat dissipation. The concurrent appearance of impurity related secondary phases correlates with distorted grain morphology in Figure 4(e), reinforcing the conclusion that lower scan speeds intensify texture anisotropy and possibly contribute to direction dependent mechanical responses.

## 4 Conclusions

This study investigated the influence of scanning speed on the microstructure, phase formation, and crystallographic texture of Al-Si-Mg alloys printed via PBF-LB. The key findings are summarized as follows:

1. The microstructural evaluation revealed distinct differences in porosity and fusion attributes across all scanning speeds. Sample A (1815 mm/s) showed the highest porosity (0.85%) with a mean pore size of 0.224 μm, linked to incomplete fusion and unmolten regions. Sample B (1732 mm/s) recorded the lowest porosity (0.27%) and the smallest mean pore size (0.057 μm), reflecting improved fusion quality at intermediate energy input. Sample C (1650 mm/s) exhibited moderate porosity (0.48%) but the largest pores (1.326 μm), suggesting unstable melt pool dynamics. Sample D (1567 mm/s) and E (1485 mm/s) exhibited comparable porosities of 0.37% and 0.34%, with mean pore sizes of 0.233 μm and 0.198 μm, respectively, reflecting more uniform fusion but persistent subsurface defects. Overall, defect density is highly sensitive to scanning speed, with Sample B offering favourable defect reduction.
2. Grain structure analysis revealed that scanning speed strongly influences solidification behaviour and eutectic silicon morphology. Higher speeds (Samples A and B) led to elongated grains and irregular eutectic networks due to melt pool instability and localized thermal fluctuations. Sample C exhibited refined columnar grains and interconnected silicon networks, suggesting optimal thermal gradients. Further reduction in speed (Samples D and E) resulted in more continuous and compact eutectic silicon networks and strong directional solidification along the build direction, consistent with increased energy input and slower cooling rates.
3. Phase analysis confirmed the α-Al matrix as the dominant phase across all scanning speeds, with secondary phases such as $Mg_2Si$, iron oxides, and, in some cases, trace impurities like Ru and Pb-based compounds. The appearance of these phases is attributed to oxidation, residual oxygen within the chamber atmosphere, improper powder handling,

and redeposition of spatter particles, all of which can introduce impurities into the melt pool. The presence of increased secondary phase formation evident at lower scan speeds, aligning with SEM observations of eutectic formation and remelting regions.

4. Crystallographic texture analysis further highlighted the impact of scanning speed. High scanning speeds produced broader and less defined diffraction peaks, indicating strain-induced microstructural distortion and residual stress. As the scanning speed decreased, the diffraction patterns revealed sharper and more intense α-Al peaks, particularly in Sample E, confirming a stronger preferential orientation and directional solidification. The highest degree of texture anisotropy and residual stress accumulation was observed at the lowest scanning speed, likely resulting from sustained heat input and slower cooling rates.

In summary, this study shows that scanning speed in PBF-LB exerts a decisive influence on porosity, microstructure, phase formation, and crystallographic texture in Al-Si-Mg alloys. The highest scanning speed (Sample A, 1815 mm/s) produced the greatest porosity (0.85%) from incomplete fusion, while Sample B (1732 mm/s) achieved the lowest porosity (0.27%) and finest defect distribution. At 1650 mm/s (Sample C), porosity was moderate (0.48%) but accompanied by the largest pore size (1.326 µm) highlighting melt pool instabilities despite a relatively refined eutectic network. Lower scanning speeds (Samples D and E, 1567 and 1485 mm/s) promoted dense eutectic silicon networks and pronounced columnar grains but introduced secondary phases. A desirable as-built microstructure was defined by refined eutectic networks, aligned α-Al grains, and minimized porosity. Based on this, Sample B offered the best defect minimization, while Samples D and E exhibited superior microstructural refinement. Overall, scanning speed controls a balance between defect minimization and microstructural refinement, and the as-built microstructures remain amenable to post-processing for further optimization.

## References

1. ISO/ASTM. (2021). ISO/ASTM 52900:2021 - Additive manufacturing — General principles — Fundamentals and vocabulary.
2. P. Ashwath, M.A. Xavior, A. Batako, P. Jeyapandiarajan, J. Joel. Selective laser melting of Al–Si–10Mg alloy: microstructural studies and mechanical properties assessment. *Journal of materials research and technology*, (2022) **17**, pp.2249-2258.
3. G. Di Egidio, A. Morri, L. Ceschini, L. Tonelli. High-Temperature behavior of the heat-treated and overaged AlSi10Mg alloy produced by Laser-Based Powder Bed Fusion and comparison with conventional Al-Si-Mg casting alloys. *Advanced engineering materials*, Volume 25, 2023, 2201238. https://doi.org/10.1002/adem.202201238
4. J. R. Davis. Aluminum and aluminum alloys. *ASM International* (2002).
5. A. Paraschiv, G. Matache, M.R. Condruz, T.F. Frigioescu, L. Pambaguian. Laser Powder Bed Fusion Process Parameters' Optimization for Fabrication of Dense IN 625. *Materials (Basel)*. 2022 Aug 21;15(16):5777. doi: 10.3390/ma15165777. PMID: 36013913; PMCID: PMC9414232.
6. W. Pan, Z. Ye, Y. Zhang, Y. Liu, B. Liang, Z. Zhai. Research on Microstructure and Properties of AlSi10Mg Fabricated by Selective Laser Melting. *Materials*. 2022; **15**(7):2528. https://doi.org/10.3390/ma15072528
7. N.T. Aboulkhair, M. Simonelli, L. Parry, I. Ashcroft, C. Tuck, R. Hague, 3D printing of Aluminium alloys: Additive Manufacturing of Aluminium alloys using selective

laser melting, *Progress in Materials Science*, Volume **106**, 2019, 100578, https://doi.org/10.1016/j.pmatsci.2019.100578.

8. H. Azizi, A. Ebrahimi, N. Ofori-Opoku, M. Greenwood, N. Provatas, & M. Mohsen. Solidification Characteristics of Laser-Powder Bed Fused AlSi10Mg: Role of Building Direction. *arXiv*, (2020). https://arxiv.org/abs/2003.09757
9. A. Hadadzadeh, B.S. Amirkhiz, S. Shakerin, J. Kelly, J. Li, M. Mohammadi, Microstructural investigation and mechanical behavior of a two-material component fabricated through selective laser melting of AlSi10Mg on an Al-Cu-Ni-Fe-Mg cast alloy substrate, *Additive Manufacturing*, Volume **31**, 2020, 100937, https://doi.org/10.1016/j.addma.2019.100937.
10. J. Wu, X. Q. Wang, W. Wang, M. M. Attallah, and M. H. Loretto. Microstructure and strength of selectively laser melted AlSi10Mg," *Acta Materialia*, (2016) vol. **117**, pp. 311–320, doi: https://doi.org/10.1016/j.actamat.2016.07.012.
11. J. E. Cobbinah, and S. E. Oduro Controlled Crystallographic Texture Orientation in Structural Materials Using the Laser Powder Bed Fusion Process—A Review. *Advanced Engineering Materials*, 2023 **25**(9), 2300819. https://doi.org/10.1002/adem.202300819
12. F. Sun, P. Liu, W. Liu. Multi-level deep drawing simulations of AA3104 aluminium alloy using crystal plasticity finite element modelling and phenomenological yield function. *Advances in Mechanical Engineering*. 2021;13(3). doi:10.1177/16878140211001203
13. V. Romanova, A. Borodina, E. Dymnich, V. Balokhonov, R. Balokhonov. Influence of cellular dendritic structure and grain orientation on deformation behavior of additively manufactured AlSi10Mg alloy. *Russ Phys J* **67**, 1668–1676 (2024). https://doi.org/10.1007/s11182-024-03296-w
14. M.M. Pariona. Effects of the Aluminum Alloy with Intermetallic a Phase on the Microstructural and Corrosion Resistance. *Int J Robot Eng* 6:035 (2021). DOI: 10.35840/2631-5106/4135
15. E. Weidmann and A. Guesnier," Metallographic preparation of aluminium and aluminium alloys," Struers application notes
16. F.H. Kim, S.P. Moylan. Literature review of Metal Additive Manufacturing Defects. *NIST Advanced Manufacturing Series* 100-16, (2018). https://doi.org/10.6028/NIST.AMS.100-16
17. D. Basu, Z. Wu, J.L.L Meyer, et al. Entrapped Gas and Process Parameter-Induced Porosity Formation in Additively Manufactured 17-4 PH Stainless Steel. *J. of Materi Eng and Perform* **30**, 5195–5202 (2021). https://doi.org/10.1007/s11665-021-05695-3
18. Y. Huang, T.G. Fleming, S.J. Clark, S. Marussi, K. Fezzaa, J. Thiyagalingam, C.L.A. Leung, P.D. Lee. Keyhole fluctuation and pore formation mechanisms during laser powder bed fusion additive manufacturing. *Nat Commun.* 2022 Mar 4;13(1):1170. doi: 10.1038/s41467-022-28694-x
19. L. Wang, S. Feng, Y. Wang, et al. Porosity defects in additively manufactured metal materials: Formation mechanisms, impact on performance and regulation. *International Materials Reviews*. 2025;0(0). doi:10.1177/09506608251371459
20. M. Laleh, A. E. Hughes, S. Yang, J. Wang, J. Li, A. M. Glenn, W. Xu, M. Y. Tan. A critical insight into lack-of-fusion pore structures in additively manufactured stainless steel, *Additive Manufacturing*, Volume 38, 2021, 101762,https://doi.org/10.1016/j.addma.2020.101762.

21. H. B. Nasrabadi, U. E. Klotz, D. Tiberto, *et al.* Effect of keyhole and lack-of-fusion pores on the anisotropic microstructure and mechanical properties of PBF-LB/M-produced CuCrZr alloy. *Prog Addit Manuf* **10**, 6295–6309 (2025). https://doi.org/10.1007/s40964-025-00972-2
22. AH Maamoun, YF Xue, MA Elbestawi, SC Veldhuis. The Effect of Selective Laser Melting Process Parameters on the Microstructure and Mechanical Properties of Al6061 and AlSi10Mg Alloys. *Materials*. 2019; **12**(1):12. https://doi.org/10.3390/ma12010012
23. K.G. Prashanth, J. Eckert, Formation of metastable cellular microstructures in selective laser melted alloys, *Journal of Alloys and Compounds*, Volume **707**, 2017, Pages 27-34, https://doi.org/10.1016/j.jallcom.2016.12.209.
24. X. Liu, C. Zhao, X. Zhou, Z. Shen, W. Liu, Microstructure of selective laser melted AlSi10Mg alloy, *Materials & Design*, Volume **168**, 2019, 107677, https://doi.org/10.1016/j.matdes.2019.107677.
25. M. Balbaa, M. Elbestawi. Multi-Scale Modeling of Residual Stresses Evolution in Laser Powder Bed Fusion of Inconel 625. *Journal of Manufacturing and Materials Processing*. 2022; 6(1):2. https://doi.org/10.3390/jmmp6010002
26. I. Serrano-Muñoz, T. Mishurova, T. Thiede, M. Sprengel, A. Kromm, N. Nadammal, et al. The residual stress in as-built Laser Powder Bed Fusion IN718 alloy as a consequence of the scanning strategy induced microstructure. *Sci Rep **10**, 14645 (2020).* https://doi.org/10.1038/s41598-020-71112-9.
27. S. Chowdhury, N. Yadaiah, C. Prakash, S. Ramakrishna, S. Dixit, L. R. Gupta, D. Buddhi, Laser powder bed fusion: a state-of-the-art review of the technology, materials, properties & defects, and numerical modelling, *Journal of Materials Research and Technology*, Volume **20**, 2022, Pages 2109-2172, https://doi.org/10.1016/j.jmrt.2022.07.121.
28. Y. Bresson, A. Tongne, M. Baili, *et al.* Identifying main contamination factors of laser powder bed fusion oxidation-sensitive powders. *Int J Adv Manuf Technol* **127**, 2687–2706 (2023). https://doi.org/10.1007/s00170-023-11239-x